Nanocrystallization kinetics and glass forming ability of the $Fe_{65}Nb_{10}B_{25}$ metallic alloy

J. Torrens-Serra,* J. Rodríguez-Viejo, and M. T. Clavaguera-Mora
Grup de Nanomaterials i Microsistemes, Departament de Física, Universitat Autònoma de Barcelona, Edifici Cc, 08193 Bellaterra, Spain

(Received 21 March 2007; revised manuscript received 2 August 2007; published 19 December 2007)

The crystallization kinetics of glassy $Fe_{65}Nb_{10}B_{25}$ melt-spun ribbons is studied by differential scanning calorimetry in the mode of continuous heating and isothermal annealing and by x-ray diffraction and transmission electron microscopy. Continuous heat treatments of the ribbons show the presence of multiple exothermic peaks before melting. The low-temperature peak corresponds to the precipitation of nanoscale $Fe_{23}B_6$-type crystalline metastable phase, and further annealing leads to its transformation into the metastable Fe_3B phase and subsequent formation of bcc-Fe, Fe_2B, and FeNbB stable crystalline phases. The nucleation frequency and the growth rate are determined at selected temperatures from the analysis of the microstructures that emerge during the $Fe_{23}B_6$-type nanocrystallization. The *master curve* method is used to obtain the apparent activation energy and the Avrami exponent at the nanocrystallization onset. The nanocrystallization kinetics is explained in the framework of the Kolmogorov-Johnson-Mehl-Avrami theory. The rejection of insoluble alloy atoms during primary crystallization, the formation of diffusion layers around the crystals, and the decrease in the nucleation frequency caused by alloy enrichment of the residual disordered matrix is modeled through a soft impingement factor. Estimated values for the interfacial energy that provide a satisfactory agreement between experiments and modeling are derived considering that homogeneous nucleation frequency and interface-controlled grain growth are dominant at the onset of the nanocrystallization. Consequently, the time-temperature-transformation diagram is also drawn and the critical cooling rate estimated for this glass forming alloy.

DOI: 10.1103/PhysRevB.76.214111 PACS number(s): 81.05.Kf

I. INTRODUCTION

Bulk metallic glasses (BMGs) are becoming a novel class of materials with unique physical properties that can be exploited for structural and functional applications.[1,2] These metallic glasses require a relatively low critical cooling rate R_c and show the glass transition at the temperature T_g, followed by a supercooled liquid region before crystallization occurs. Many families of multicomponent glass forming alloys—viz., Mg-, Ln- (Ln=lanthanide metals), Zr-, Fe-, Pd-, Cu-, Ti- and Ni-based alloys,[1,3]—exhibit excellent glass forming ability. Typical critical cooling rates range between 10^{-1} and 10^3 K s^{-1} and the reduced glass transition temperature T_g/T_m have a value of about 0.65, T_m being the melting temperature. The glass formation, the structure upon crystallization, and the magnetic properties of glassy ribbons of the Fe-Nb-B ternary alloys have been studied for the consecution of good soft magnetic materials.[4] To enhance thermal stability and glass forming ability (GFA) different transition metals and/or rare earth elements are included as additives.[5–7] Good nanostructured soft magnetic Fe-Nb-B-based materials nowadays used commercially have been developed using a high content of Fe (>80%) and a low content of B (<15%).[2,8–11] Also, alloys with <70 at. % Fe and >25 at. % B are the base for the development of multicomponent BMGs.[12–15] The first calorimetric event that suppresses the amorphous state is the precipitation of nanograins from the amorphous matrix, so the study of nanocrystallization kinetics becomes fundamental in order to understand the thermal stability. Since the transformed crystalline fraction as a function of time and temperature is generally described by the Kolmogorov-Johnson-Mehl-Avrami (KJMA) theory,[16–18] the differential scanning calorimetric (DSC) kinetic analysis leads, traditionally, to an estimation of both the apparent activation energy E_a and the local Avrami exponent n as a function of the transformed fraction.[19–22] Recently, a new method, called the master curve method (MCM), has been developed for the analysis of the kinetic data obtained from DSC.[23,24] The method applies provided the transformation rate can be expressed in terms of a first-order separable differential equation, with an Arrhenius temperature dependence of the rate constant (or, equivalently, of the nucleation and growth rates). The obtained master curve is the average of all the experimental continuous heating DSC scans and has a better signal/noise ratio than the individual curves. Consequently, this method allows obtaining a precise value of E_a and will be used in the present study.

Although the calorimetric analysis provides critical kinetic information about the overall crystallization process, it fails to deliver a description of individual processes of nucleation and growth. Thus, a corresponding microstructural examination is also necessary to fully describing the phase transformation within the KJMA formalism. In primary crystallization the situation becomes much more complicated due to the independent variations of the nucleation and growth rate with temperature and matrix solute content.[25]

In this paper we report on a detailed study of the nanocrystallization kinetics, GFA, and thermal stability of $Fe_{65}Nb_{10}B_{25}$ alloys obtained by rapid solidification. This study provides an opportunity to compare kinetic parameters determined from experimental data and the theoretical modeling (KJMA, classical homogeneous nucleation, and interface-controlled growth) that were posed several decades ago. This quantitative analysis could provide groundwork for the control of microstructures obtained by thermal treatment

as well as for glass forming ability of the molten alloy. The glass formation process is discussed in terms of the thermodynamics and kinetics of the nanocrystallization process. A key kinetic parameter is the viscosity whereas the ease for glass formation should be related to both the driving force for crystallization and the liquid-crystal interfacial energy.[26,27] The transformation to a nanostructured material by thermal treatment is visualized as initiated with the formation of the primary crystals and subsequent development of a concentration gradient ahead of the nucleating front. Grounded on the nucleation and growth of the precipitates, the analysis of the evolution of the transformed fraction with time as a function of the thermal treatment is here performed beyond the constant activation energy assumption.

The structure of the present paper is as follows: A simple but systematic microstructural path for crystallization of the FeNbB metallic glass is deduced from DSC and x-ray diffraction (XRD) measurements. A careful study of the primary crystallization is performed under both isothermal and continuous heating regimes. The individual nucleation and growth kinetic rates are found directly from transmission electron microscopy (TEM) observations at selected temperatures. The main objective is to establish a firm basis for modeling the primary crystallization. Therefore, we discuss the generic issues that arise in the application of the master curve method to coupled continuous heating and isothermal DSC data. The most important of these issues is that the method of analysis leads to the determination of the values of the exponent n and the individual activation energies of nucleation and growth at the onset of the transformation (where soft impingement effects can be ignored). The results of the analysis are used to assess whether the transformation follows the KJMA model with constant activation energy. However, since the constant activation energy assumption is a rough approximation only justified when considering a limited temperature range, values of the interfacial energy, viscosity, and driving force for crystallization are tentatively evaluated from nucleation and growth data at precise experimental crystallization temperatures and extrapolated to obtain the time-temperature-transformation (TTT) diagram. Glass forming ability is obtained from critical cooling rate estimations.

II. EXPERIMENTAL PROCEDURE

Glassy $Fe_{65}Nb_{10}B_{25}$ ribbons were prepared by melt spinning under Ar atmosphere with single Cu roller at a linear velocity of 40 m/s. The master alloy was prepared from Fe, Fe_2B (98% purity), and NbB (99% purity) powders, pressed at 150 kg/cm^2 and melted 3 times for 15 s in an induction furnace to improve homogeneity. The ribbons are about 20 μm thick and 2 mm wide. Both as-prepared and annealed samples were examined by XRD in a Philips xPert diffractometer using Cu $K\alpha$ radiation and by TEM providing also selected-area electron diffraction (SAED) using a Philips CM30 microscope.

DSC measurements have been performed with a NETZSCH DSC 404, for high-temperature measurements, and a Perkin-Elmer DSC7 differential scanning calorimeters under dynamic pure Ar atmosphere. Continuous heat treatments at different heating rates (2.5–80 K/min) and isothermal measurements at selected temperatures were done in the PE DSC7. The calorimeter was calibrated using Zn and K_2CrO_4 as reference materials. A second scan has been always done in order to subtract the DSC base line in both continuous heating and isothermal experiments. Annealed samples at different temperatures during 30 min for TEM observation were also prepared in the DSC7 apparatus.

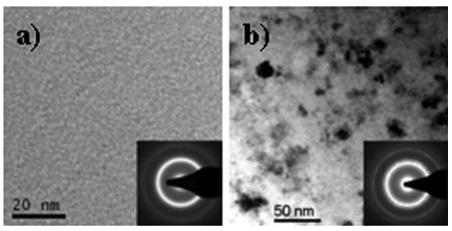

FIG. 1. TEM micrographs and corresponding SAED patterns of the sample (a) as-quenched and (b) after primary crystallization.

III. EXPERIMENTAL RESULTS

The XRD spectrum of the as-prepared sample presents the characteristic halo of an amorphous material without any crystalline peak but with a broad peak situated at $2\theta=43.7°$. Correspondingly no trace of crystallinity can be observed in both TEM images and SAED patterns [Fig. 1(a)].

Figure 2 shows the DSC heating curve at 10 K/min up to 1200 K; it shows a glass transition at $T_g=862$ K followed by three exothermic peaks. The first peak, with onset at $T_x=913$ K and maximum transformation rate at $T_{p1}=920$ K, has an asymmetric shape with a very sharp beginning and a slowdown of the transformation rate in the last stage of transformation. The supercooled liquid interval $\Delta T_x=T_x-T_g$, has a value of 51 K. The large supercooled region preceding devitrification has been previously observed in these types of alloys[7,12] and the first peak was assigned to the primary crystallization of nanocrystals in an amorphous matrix. It is also

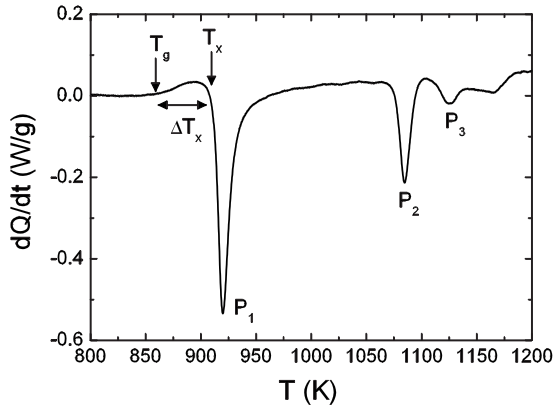

FIG. 2. DSC scan at 10 K/min up to 1200 K. P_1, P_2, and P_3: first, second, and third crystallization peaks. T_g, glass transition temperature; T_x temperature onset of the first crystallization peak; ΔT_x, supercooled liquid interval.

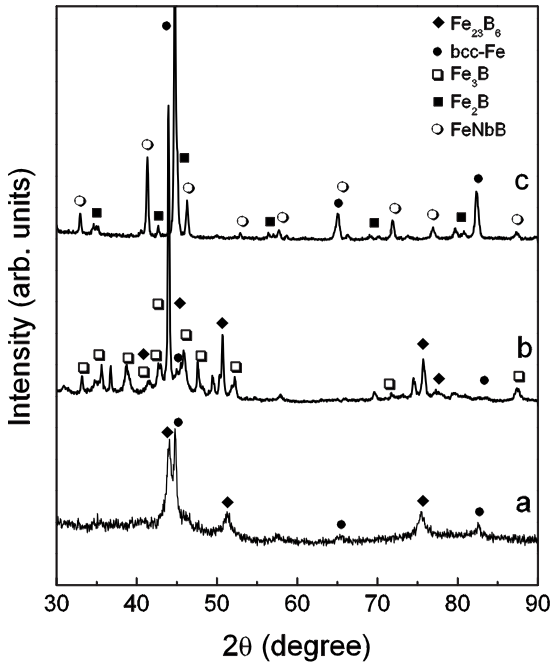

FIG. 3. X-ray diffraction pattern after continuous heating at 10 K/min up to (a) 990 K, (b) 1103 K, and (c) 1273 K.

interesting to note that values of ΔT_x in the range 25–65 K have been reported for different bulk amorphous alloy systems with four, five and six nonmagnetic components added to ferromagnetic Fe.[2] The second peak has a maximum at $T_{p2}=1085$ K and the last peak shows a maximum at $T_{p3}=1124$ K. At higher temperatures an endothermic peak, at $T_E=1414$ K, attributed to the eutectic transformation is observed.

Figure 3 shows the XRD patterns of room temperature samples previously heated up to temperatures beyond the three exothermic DSC peaks at 10 K/min. XRD analysis shows that the first crystallization peak (see spectrum *a* in Fig. 3) is associated with the formation of a $Fe_{23}B_6$-like cubic structure, as main crystallization product, and bcc-Fe with a remaining amorphous matrix. This metastable boride has been previously found in Fe-Nb-B alloys and its formation is induced by the addition of Nb in the Fe-B system.[5,7,28] The TEM investigations show a primary crystallization consisting in the formation of nanocrystals. Suzuki *et al.*[11] observed for FeNbB alloys with a Nb content higher than 6 at. % a grain size not larger than 15 nm. This limitation arises from the piled Nb atoms in the grain boundary stopping the grain growth. The SAED pattern [Fig. 1(b)] shows the diffraction circles corresponding to the randomly oriented nanocrystalline phase. The bcc Fe precipitates appear at the latest stages of the primary crystallization, as observed in isothermal experiments by XRD (see Fig. 4), but its presence is not confirmed by the results of SAED and transmission Mössbauer spectroscopy.[29] This phase was also previously observed by Shapaan *et al.*[7] but not by Imafuku *et al.*[5] for similar compositions. In the second crystallization peak the precipitation of the metastable Fe_3B-orthorhombic boride is observed [Fig. 3(b)] while $Fe_{23}B_6$ is still present (has not yet decomposed). Finally, the third peak is attributed to the

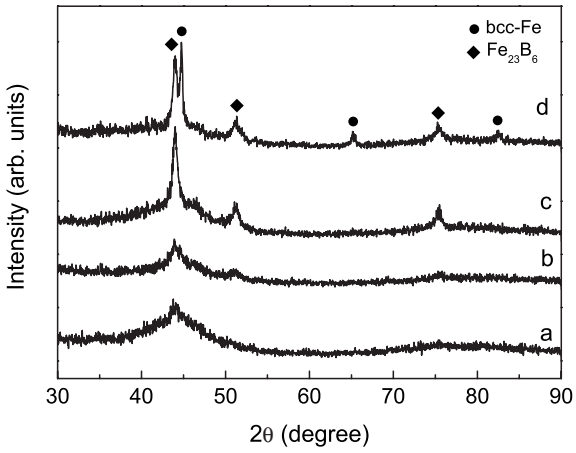

FIG. 4. X-ray diffraction patterns after isothermal annealing at 893 K during (a) 5 min, (b) 7.5 min, (c) 20 min, and (d) 60 min.

decomposition of the metastable phases into bcc Fe, Fe_2B, and FeNbB [Fig. 3(c)], which correspond to the equilibrium phases in the ternary phase diagram.[30] That is, in this alloy the metastable borides $Fe_{23}B_6$ and Fe_3B precipitate successively in two stages and decompose before the melting temperature is reached. The formation of Fe_2B in the last transformation was also reported in Refs. 5 and 7.

To study the primary crystallization kinetics, calorimetric scans from 2.5 to 80 K/min and isothermal DSC measurements at 898, 903, and 908 K have been performed and are shown in Figs. 5 and 6, respectively. The nanocrystallization enthalpy and heat capacity change at the glass transition were evaluated from the DSC curves $\Delta H=-(100\pm5)$ J/g, $\Delta C_p=(0.32\pm0.05)$ J/(K g). (Note that both ΔH and $d\Delta H/dT$—or $d\Delta H/dt$—are negative for crystallization; i.e., heat is released). As can be seen in Figs. 5 and 6, part of the uncertainty of the ΔH value is due to the random base line drift observed over a large temperature interval (see, in Fig. 5, the differences in the two recorded signals, dashed and solid lines, plotted for every scan rate). This uncertainty is more pronounced when the signal extends over a very long time range in isothermal measurements (see, in Fig. 6, the last part of the signal, almost outside the time range where crystallization occurs). In the isothermal annealing experi-

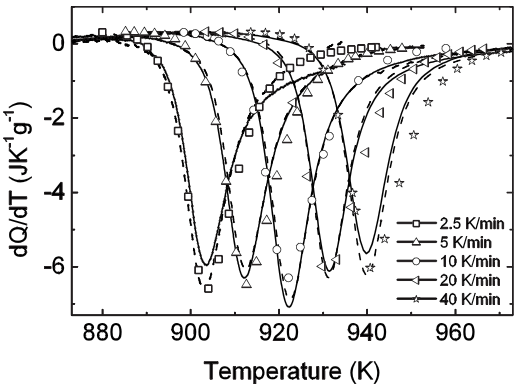

FIG. 5. DSC continuous heating scans as measured (dashed and solid lines, two different scans) and fitted values using the constant activation energy KJMA kinetic model (symbols).

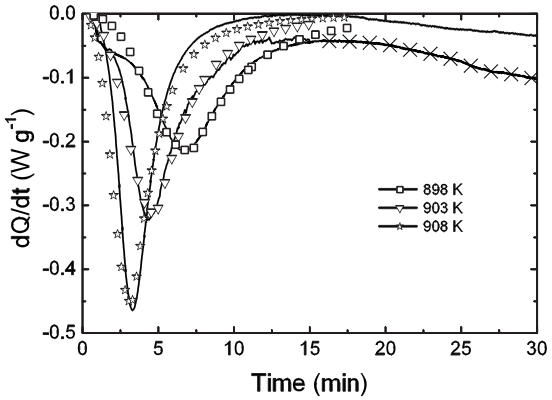

FIG. 6. DSC isotherms at temperatures of 898, 903, and 908 K. Solid lines: as measured Dashed-cross lines: base line drift at long time range. Symbols: as fitted using the constant activation energy KJMA kinetic model.

ments, other sources of error come from the uncertainty associated with the determination of the exact positions of the onset of the exotherm and to any transient signal resulting from the changing from continuous heating to isothermal regime (see Fig. 6). These factors limit the temperature interval where significant DSC isothermal measurements can be performed and, probably, are the main reasons why scarce data on DSC isothermal nanocrystallization are reported in the literature for Fe-Nb-B metallic glasses.

The development of crystalline grains on samples annealed at 873 K and 883 K for 30 min has been analyzed by TEM. Although an analysis of TEM images is not straightforward, it gives an interesting qualitative overview of the developed microstructure and morphological results have been very valuable for characterizing the beginning of the transformation. In particular, the nucleation frequency I and crystal growth rate u were estimated from multiple TEM micrographs, such as those presented in Figs. 7(a) and 7(b). The morphology of the precipitates shown in Fig. 7 is representative of the whole sample. Neither preferential orientation nor anisotropic shape is observed in the precipitates. Comparison between the two samples shows that in the sample annealed at 873 K the precipitates are clearly isolated and small, while in the sample annealed at 883 K the number of precipitates has increased and some of them have larger size and sometimes overlap. The overall picture shows that particles seem to nucleate randomly and to grow isotropically. Neglecting particle overlapping and assuming a 50-nm-thick observed zone, the maximum grain size and surface grain density are evaluated and given in Table I, as well as the values estimated for the nucleation frequency and crystal growth rate. The experimental uncertainty includes

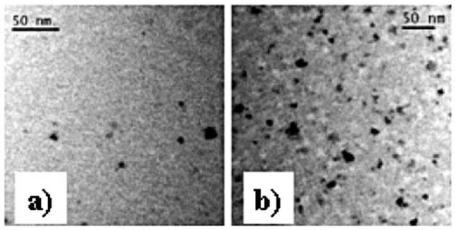

FIG. 7. TEM micrographs of the sample annealed (a) at 873 K during 30 min and (b) at 883 K during 30 min.

the consideration that the sample thickness is not constant, the possible overlapping of particles, and the limitations of the projection of a three-dimensional body on a two-dimensional image.[31] Like for continuous heated samples, the XRD patterns on these isothermally annealed samples show mainly the precipitation of a $Fe_{23}B_6$-type structure. In agreement with findings by other authors,[11] the results presented in Table I indicate a high homogeneous nucleation rate in the supercooled liquid region as well as a retarded growth rate, most likely induced by a large redistribution of Nb among the primary crystallites and the disordered matrix.

IV. DISCUSSION

In the present study our attention is focused on the kinetics of primary crystallization of $Fe_{23}B_6$-type crystals from the disordered matrix. Aside from examining the apparent activation energy of the overall process and the behavior of the local Avrami exponent as a function of the crystalline volume fraction, a detailed analysis of the kinetic quantities that drive the process is also carried out. The glass forming ability and thermal stability of this alloy are tentatively quantified.

The DSC continuous heating curve (Fig. 5) shows a primary crystallization peak superposed with a significant heat capacity change $(-\Delta C_p)$ during the transformation: the heat capacity of the sample shifts gradually from the heat capacity of the undercooled melt to the heat capacity of the nanostructured material. That is, assuming an ideal mixing enthalpy of the undercooled melt,[32] the overall exothermic DSC signal dQ/dt is shared between the instantaneous crystallization enthalpy change $d\Delta H/dt$, which is proportional to the transformation rate $d\alpha/dt$ or dx/dt (where $\alpha=f_1x$ with f_1 the final primary volume fraction and x the scaled transformed fraction), and the heat capacity contribution $dQ_{\Delta Cp}/dt$, which is proportional to the transformed volume fraction α (considering that the overall specific heat of the specimen is given by the linear interpolation of the specific heats of the undercooled melt and the crystalline compound). Using the scaled

TABLE I. Estimated values of the surface grain density n_s, nucleation frequency I, maximum grain size D_{max}, and growth rate u at two different annealing temperatures.

T_{iso} (K)	n_S (cm^{-2})	I (cm^{-3} s^{-1})	D_{max} (cm)	u (cm s^{-1})
873	$(4.5\pm1.9)\times10^{10}$	$(4.9\pm3.5)\times10^{12}$	$(12.6\pm1.0)\times10^{-7}$	$(3.5\pm0.6)\times10^{-10}$
883	$(1.0\pm0.1)\times10^{11}$	$(1.1\pm0.7)\times10^{13}$	$(23.6\pm1.0)\times10^{-7}$	$(6.6\pm0.6)\times10^{-10}$

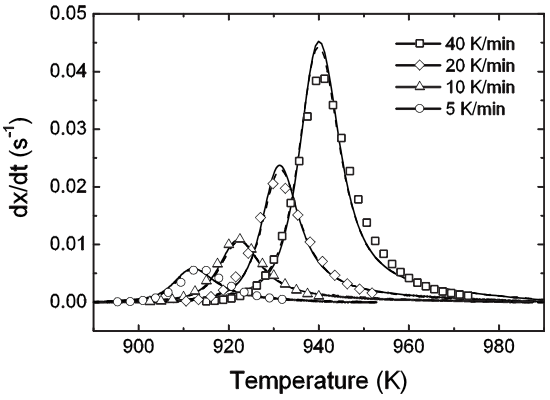

FIG. 8. Transformation rate under continuous heating as measured (dashed and solid lines, two different scans) and fitted values using the nucleation/growth KJMA formalism (symbols).

quantities dx/dt and x, the relationship between these quantities is given by

$$\frac{dQ}{dt} = \frac{d\Delta H}{dt} + \frac{\Delta C_p dT}{dt} x = \Delta H \frac{dx}{dt} - \beta \Delta C_p x, \tag{1}$$

where β is the heating rate. These two contributions to the signal were separated using an iterative procedure,[33,34] and the resulting transformation rate is plotted against temperature for different heating rates in Fig. 8.

Once the transformation rate is known, the modeling of the primary crystallization kinetics is grounded on the KJMA formalism. Since the transforming phase ($Fe_{23}B_6$) has a different composition from the matrix, the kinetics of the transformation depends on the diffusion and redistribution of solute atoms (soft impingement). Following the classical treatment the contribution of (geometrical) impingement of growing grains is considered through the KJMA formalism, while the influence of diffusion on the growth rate is modeled by an initial interface-controlled growth that becomes progressively diffusion controlled growth.[25] To explore the evolution of the soft impingement in primary crystallization, in a first stage, simple thermally activated forms of the nucleation frequency, the interface-controlled crystal growth, and the diffusion coefficient of the solute are assumed in the computation. This is realistic considering that the primary crystallization data are explored in a range of 100 K (between about 885 and 960 K) whereas the supercooled molten alloy is metastable in a much wider range (between about 800 and 1400 K). In order to understand the mechanisms that drive the process, in a second stage, the restriction of constant activation energy is released and both nucleation frequency and interface-controlled crystal growth are linked to thermodynamic (free energy and interfacial energy) and kinetic (mainly viscosity) quantities. Then tentative TTT diagrams in the range 800–1000 K are constructed and the critical cooling rate required for this alloy to form glass upon quenching is estimated.

A. Constant KJMA activation energy model

1. Determination of the apparent activation energy

In the conventional KJMA framework, under isothermal annealing at temperature T_{iso}, imposing an Arrhenian temperature dependence for both nucleation and growth rate, the transformation rate (dx/dt) may be expressed in terms of the Avrami exponent n as

$$\frac{dx}{dt} = \frac{\exp\left(\frac{-E_a}{kT_{iso}}\right)}{P_{iso}(x)}, \tag{2}$$

with

$$P_{iso}(x) = \frac{P_{0,iso}[-\ln(1-x)]^{(1-n)/n}}{n(1-x)}, \tag{3}$$

where x is the scaled transformed volume fraction of the primary phase, k is Boltzmann's constant, and $P_{iso}(x)$ a kinetic function dependent on the transformation mechanisms. E_a is the apparent activation energy that, in terms of the activation energies for nucleation, E_I, and growth, E_u, is given by

$$E_a = \frac{E_I + (n-1)E_u}{n} \tag{4}$$

for a $(n-1)$ dimensional growth.

It has been recently shown[35,36] that under continuous heating at a constant rate β, the equivalent form of Eq. (2) gives the transformation rate (dx/dT) as

$$\frac{dx}{dT} = \frac{\exp\left(\frac{-E_a}{kT}\right)}{\beta P(x)}, \tag{5}$$

with

$$P_{iso}(x) = C(n, E_I, E_u) P(x), \tag{6}$$

C being a scaling factor dependent on the Avrami exponent n and both activation energies for nucleation, E_I, and growth, E_u.

Interestingly, apart from the factor C, a unique functional dependence on x [$P(x)$ or $P_{iso}(x)$] describes both continuous heating and isothermal transformation rate in the form given by Eqs. (2) and (5).

To minimize the inherent experimental inaccuracies in kinetics studies, the apparent activation energy was determined through the application of the MCM[23,24] to the DSC continuous heating data. The set of transformation rate curves obtained at different heating rates has been translated into a unique equivalent heating rate following the procedure described in Ref. 24. The *master curve* has been obtained as the average of the set of translated continuous heating transformation rate curves. Consequently, most of the systematic errors of the individual dx/dT curves disappear in the averaging procedure. This methodology not only provides a value of E_a that fits the overall transformation process but it also conducts straightforward to the function $P(x)$. Figure 9 shows the master curve at 10 K min^{-1} obtained from DSC data at 5, 10, 20, 40, and 80 K min^{-1}. The apparent activation energy was determined with the best overlapping of the experimental data in the master curve and its value is $E_a = 5.27$ eV. This value for the apparent activation energy is typical for Fe-Nb-B alloys[7,37] but higher than those found for

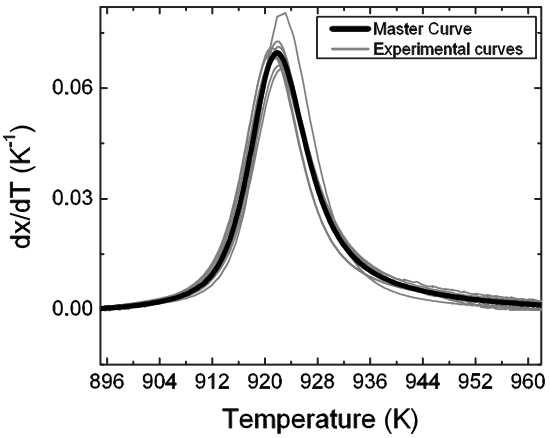

FIG. 9. Master curve (black line) and experimental curves (gray thin lines) at an equivalent heating rate of 10 K/min.

nanocrystallization in other systems where only grain growth from embryos is observed,[2,23] indicating that homogeneous nucleation plays an important role in the primary crystallization of the studied alloy. Figure 10 shows the plot of $P^{-1}(x)$ against x obtained from the master curve when the above value of the apparent activation energy is introduced in Eq. (5). Note that the plot is restricted to values of $0.02 \leqslant x \leqslant 0.92$ to avoid the uncertainty associated with the determination of the reaction rate at the onset and the end of the transformation.

2. Coupling of isothermal and continuous heating data

According to Eq. (6), the coupling of experimental data in both regimes allows the relationship between n, E_I, and E_u to be determined. Furthermore, integration of Eq. (3) gives

$$G_{iso}(x) = \int_0^x P_{iso}(x)dx = P_{0,iso}[-\ln(1-x)]^{1/n}. \tag{7}$$

That is, $P_{0,iso}$ may be interpreted as a characteristic time depending on the detailed mechanisms driving the transformation (see, for instance, Ref. 24).

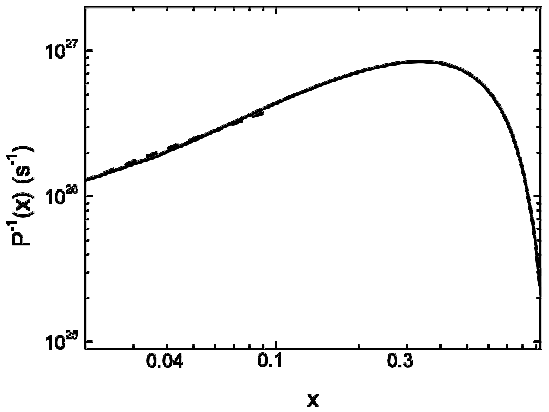

FIG. 10. Plot of $P^{-1}(x)$ versus x obtained from the experimental continuous heating DSC data using the master curve (solid line) and Avrami fit between $2\% < x < 8\%$ with $n=4$ (dashed line).

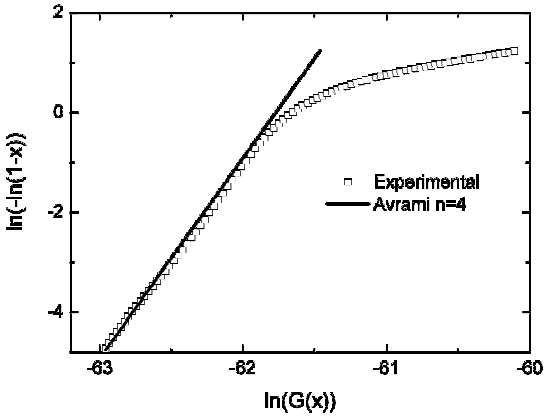

FIG. 11. $G(x)$ function obtained by integration of $P(x)$ (squares). The solid line corresponds to the asymptotic fit of the $P(x)$ function at the onset of the transformation.

From Eqs. (3) and (6) it follows that we can compare the experimental $P(x)$ function to the KJMA model. The tentative fit of the asymptotic behavior at the beginning of the transformation with a fixed value of the Avrami exponent is plotted in Fig. 10. Equivalently, we obtained by integration the experimental $G(x)$ function, defined by

$$G(x) = \int_0^x P(x)dx, \tag{8}$$

extrapolating the asymptotic behavior observed experimentally at the onset of the transformation. The result is shown in Fig. 11 where $\ln\{-\ln(1-x)\}$ is plotted against $\ln\{G(x)\}$. This plot is equivalent to the widely used *Avrami plot* [plot of $\ln\{-\ln(1-x)\}$ versus the logarithm of isothermal time], but obtained from continuous heating data: in both plots—as obtained from Eqs. (6)–(8)—the slope of the curve is the Avrami exponent.

Close inspection of the results plotted in Figs. 10 and 11 indicates that the local Avrami exponent is equal to 4 at the beginning of the transformation and decreases continuously as the reaction proceeds. It becomes even less than 1 for $x > 0.5$.

Let us explore more carefully the application of the master curve method to coupled continuous heating and isothermal DSC data. For $n=4$ (constant nucleation and interface-controlled three-dimensional growth) considering the temperature dependence of the nucleation frequency I and crystal growth u of the form

$$I(T) = I_o \exp\left(-\frac{E_I}{kT}\right), \tag{9}$$

$$u(T) = u_o \exp\left(-\frac{E_u}{kT}\right), \tag{10}$$

one obtains that

$$P_{0,iso} = \left[\frac{3f_1}{\pi I_o u_o^3}\right]^{1/4} \tag{11}$$

and the factor C depends only on the ratio $y = E_I/E_u$—i.e.,

$$C(n=4,E_I,E_u)=\Psi(E_I/E_u), \tag{12}$$

with[35]

$$\Psi^4(y)=3(3+y)^3\left[1-\frac{2y}{(1+y)}+\frac{y}{(2+y)}\right]\frac{1}{4^3y}. \tag{13}$$

It follows that the predicted KJMA $P_{\rm iso}(x)$ kinetic function may be compared to that derived from continuous heating kinetic experimental data. The onset of the transformation $(0.02<x<0.08)$ agrees with the KJMA model with a constant Avrami exponent $n=4$ and the value $P_0=P_{0,iso}/\Psi(E_I/E_u)=1.488\times10^{-27}$ s for the characteristic time. Therefore, nanocrystallization of this metallic glass proceeds via nucleation and growth of the $Fe_{23}B_6$-type primary phase under nonequilibrium conditions. In the early stages of the transformation the emerging nuclei are surrounded by a supersaturated matrix and growth is interface controlled. At intermediate stages the system may be visualized as a polydisperse mixture of precipitates of various sizes in a matrix progressively enriched from atoms insoluble in these grains. At these stages, the nucleation frequency and growth rate will no longer be a simple function of temperature due to the matrix compositional changes.[25] Since the nuclei form because of localized compositional fluctuations, the nucleation rate progressively decreases with the degree of supersaturation. The interplay between interface and diffusion-limited growth acts in such a way as to increase the importance of the last mechanism until it becomes preponderant. In the final stages of nanocrystallization $(x>0.7)$ the experimental kinetic function $P(x)$ might be approached by an Avrami function with $n\approx0.45$. A decrease in the local Avrami exponent reaching values smaller than unity at high x in the crystallization process has often been observed and may be related to soft impingement processes,[19,23,38–41] where grain growth is kinetically slowed down, and eventually inhibited, by the low degree of supersaturation in the untransformed region. Nevertheless, there is not a general agreement to attribute the delay of the transformation kinetics and the corresponding low Avrami exponent experimentally observed in primary crystallization to the soft impingement effect.[41] Also, it has been shown that anisotropic growth can lead to a change of n.[42]

3. Transformed fraction in the constant KJMA activation energy model with soft impingement

In the KJMA formalism, the extended crystalline fraction is calculated as[43]

$$x_{ext}(t)=\frac{4\pi}{3f_1}\int_0^t I(\tau)\left[r^*+\int_\tau^t u(t')dt'\right]^3 d\tau \tag{14}$$

(r^* being the critical nucleus size) and the transformation rate as

$$\frac{dx}{dt}=(1-x)\frac{dx_{ext}}{dt}. \tag{15}$$

In an attempt to develop with a minimum of computational effort solutions that can handle soft nucleation and growth, in the present investigation the forms used to describe nucleation frequency, interface- and diffusion-controlled crystal growth, and diffusion of solute through the interface are

$$I(t)=I_{homog}(T)[\varphi\{x(t)\}]^2, \tag{16}$$

$$u(t)=\begin{cases}u_{\rm interface}(T)\varphi\{x(t)\} & \text{if } r_{\rm dif}>r_{\rm int},\\ \dfrac{D_s(T)\varphi\{x(t)\}}{r(t)} & \text{if } r_{\rm dif}<r_{\rm int},\end{cases} \tag{17}$$

and

$$D_s(T)=D_o\exp\left(-\frac{E_D}{kT}\right), \tag{18}$$

where $I_{homog}(T)$ is given by Eq. (9) and $u_{interface}(T)$ by Eq. (10). $\varphi[x(t)]$ is a soft factor used to account for the time dependence of both nucleation and growth because of the compositional changes of the matrix;[25] r_{int} and r_{dif} are the extended grain radius evaluated assuming interface- and diffusion-controlled growth, respectively; D_o and E_D are, respectively, the preexponential factor and the activation energy for the diffusion coefficient of solute in the matrix, and f_1 is the primary volume fraction at the end of the transformation.

Equation (16) takes into account the fact that the nucleation rate of the primary phase decreases with time due to the enrichment of the residual disordered matrix by the faster diffusing atoms, to which we refer as soft nucleation. The growth of the particles does not stop because of direct impingement but gradually decreases due to the overlapping of the concentration profiles. The concentration gradients surrounding the particles become progressively flatter, thus reducing the diffusion-controlled growth rate. Equation (17) takes into account the fact that the effective growth mechanism is between two limiting situations: interface-controlled growth rate just after nucleation and quasi-steady-state diffusion-controlled growth for long times. In the last situation the growth rate may be considered as[19]

$$\frac{dr}{dt}=\frac{D(T)}{r}\frac{c^*-c(t)}{c^*-c_{xt}}. \tag{19}$$

Here c^* is the matrix concentration at the particle interface, c_{xt} is the solute concentration in the crystal, and $c(t)$ is the matrix average concentration as a function of time and r the time-dependent crystal radius. Considering the conservation of solute law one obtains

$$\frac{c^*-c(t)}{c^*-c_{xt}}=f_1\varphi(x), \tag{20}$$

with

$$\varphi(x)=\frac{1-x}{1-f_1x}, \tag{21}$$

which is the soft impingement factor since it decreases linearly with the degree of supersaturation. By taking $D_s(T)=f_1D(T)$ as the effective solute diffusion coefficient, Eq. (19) is identical to Eq. (17) for $r_{dif}<r_{int}$, whereas the presence of the soft impingement factor in Eq. (17) for $r_{dif}>r_{int}$ accounts

TABLE II. Parameters used in the in the constant KJMA activation energy model.

f_1	0.4	Overall primary volume fraction
I_o	8.7×10^{51} cm^{-3} s^{-1}	Nucleation rate preexponential constant of $Fe_{23}B_6$
u_o	2.3×10^{18} cm s^{-1}	Interface-controlled crystal growth
D_o	8.0×10^{9} cm^2 s^{-1}	Solute diffusion coefficient preexponential constant
E_I	6.64 eV	Activation energy of nucleation
E_u	4.81 eV	Activation energy of interface-controlled crystal growth
E_D	4.37 eV	Activation energy of diffusion coefficient

for the decrease in the growth rate due to the depletion or enrichment in solute of the region around the precipitates.

If the correction for soft impingement is performed via Eqs. (16) and (17), Eqs. (14) and (15) become nonseparable first-order differential equations. However, at the onset of the transformation, since the soft effect is negligible, the coupling of isothermal and continuous heating DSC data is still very fruitful to obtain the value of the ratio E_I/E_u.

To do the calculation, it is assumed that the critical nucleus size r^* is negligible. There are seven quantities to be fixed: I_o, u_o, D_o, E_I, E_u, E_D, and f_1. From the calorimetric data of the overall crystallization process one estimates $f_1 \approx 0.4$. From the master curve treatment of the DSC isothermal and continuous heating experiments we know the values of E_I and E_u (or E_a and E_I/E_u) and $I_o u_o^3$ at the beginning of the primary transformation as well as the form of $P(x)$ all along the transformation. As shown in Table I, from the TEM observations we have an estimate of both the nucleation frequency and growth rate at two temperatures (873 and 883 K). These data are used to fix the values of the seven quantities mentioned above, and these are listed in Table II.

The predicted transformation rate and scaled transformed volume fraction are determined from Eqs. (14) and (15) using stepwise numerical integration in temperature-time space based on the Runge-Kutta method. The calculated DSC exothermic signal at various scans rates and temperatures in both the continuous heating and isothermal regimes are shown in Figs. 5 and 6, respectively. The constant activation energy model predicts that soft impingement becomes preponderant above $x \approx 0.35$. It may be seen that the calculated values for different heating rates remain initially close to the experimental ones but show deviations at the last stage of transformation. Nevertheless, they show reasonably good agreement considering (a) the simplicity of modeling soft impingement, (b) the likely inaccuracies in the DSC data, and (c) the neglect of the precipitation of bcc Fe at the latest stage of the primary transformation.

The growth rates and hence the maximum grain size were determined at the temperatures of 873 and 883 K. The experimental and predicted maximum grain sizes are shown in Fig. 12. The predicted values of the scaled transformed volume fraction after 30 min annealing at 873 K and 883 K are $x=0.090$ and $x=0.636$, respectively. That is, the growth rate remains almost constant up to 30 min annealing at 873 K whereas for the same annealing duration, the interplay between interface- and diffusion-controlled growth is clear when the temperature is 883 K.

B. Nucleation and growth KJMA formalism

The continuous heating evolution of the transformed fraction is very sensitive to the temperature dependence of the thermodynamic and kinetic quantities, whereas the time evolution under isothermal treatment of the transformed fraction is very sensitive to the mechanisms that control the process. Nevertheless, since the temperature interval explored in DSC experiments is rather limited, a simplified Arrhenius temperature dependence for both nucleation frequency and crystal growth rate such as the one used in the model discussed in Sec. VI A may reproduce the experimental kinetic data. To obtain more fundamental parameters such as the viscosity and the interfacial energy from the measured DSC and microstructural kinetic data of the primary crystallization it is necessary to introduce a temperature dependence based on the classical nucleation and growth theory.[43]

1. Classical nucleation and growth theory

The precipitation of a primary phase from a supercooled melt is generally related to either homogeneous or heterogeneous nucleation. The formation of bulk amorphous alloys generally has to avoid possible heterogeneous nucleation to achieve a high GFA. Therefore, the restriction to stability on heating arises from homogeneous nucleation. Within the framework of classical nucleation theory, the explicit temperature dependence of the homogeneous nucleation rate under steady-state conditions, I_{homog}, can be expressed as[43]

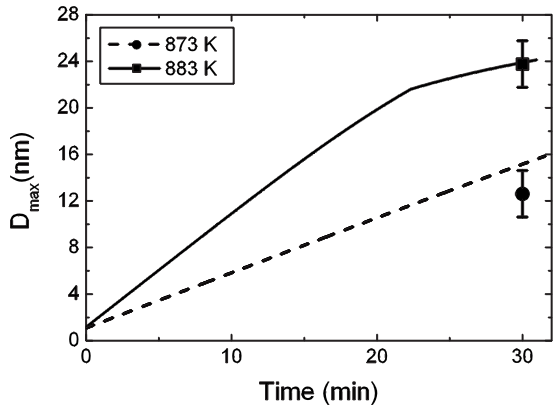

FIG. 12. Maximum diameter $D_{\max}$ as measured (symbols) and as fitted using the constant activation energy KJMA kinetic model at 873 K (dashed line) and at 883 K (solid line).

TABLE III. Parameters used in the nucleation and growth KJMA model.

V_m	6.3×10^{-6} m^3/mol	Molar volume
σ_S	{577.0–54.56T} mJ m^{-2}	Interfacial energy[a]
ΔG	{123746–12.2631T} J/mol	Gibbs free energy difference[a]
η_o	1×10^{-16} Pa s	Viscosity preexponential constant
B	46000 K	Vogel-Fulcher parameter
T_η	150 K	Vogel-Fulcher temperature

[a]With T in kelvin.

$$I=\frac{AT}{\eta}\exp\left[-\frac{16\pi\sigma^3V_m^2}{3kT(\Delta G)^2}\right], \tag{22}$$

where σ is the crystal/glass interfacial energy per unit area (surface tension), V_m is the molar volume, ΔG is the difference of the molar Gibbs free energies between glassy and crystalline phase, η is the viscosity of the melt, and A is a constant given by $A=N_vk/(3\pi a^3)$ with $N_v\cong N_A/V_m$ the number of atoms per unit volume, N_A Avogadro's number, and a the mean atomic radius $[V_m=N_A(4\pi a^3/3)]$. According to the Vogel-Fulcher-Tammann expression,[44] the temperature dependence of the viscosity can be described by

$$\eta=\eta_o\exp\left[\frac{B}{T-T_\eta}\right], \tag{23}$$

where B and T_η are empirical fitting parameters. T_η is found to lie below the experimentally observed glass transition temperature T_g. Equation (23) reveals that the viscosity of the melt depends strongly on temperature: the lower the temperature, the higher the viscosity of the melt.

Assuming fast interfacial initial growth of nuclei as far as they are small and well separated, the classical expression for the growth rate $u_{\text{interface}}$ is[43]

$$u_{\text{interface}}=\frac{CT}{\eta}\left[1-\exp\left(-\frac{\Delta G}{RT}\right)\right], \tag{24}$$

where C is a constant given by $C\cong k/(3\pi a^2)$ and R the gas constant. The relevant temperature dependences of I_{homog} and $u_{\text{interface}}$ come mainly from the temperature-dependent viscosity (it increases rapidly with decreasing temperature from fusion to the glass transition temperature) whereas I_{homog} is very sensitive to the interfacial energy values.

2. Determination of the thermodynamic and kinetic quantities

Our purpose it to obtain estimates for the viscosity, Gibbs free energy difference between the glass and the $Fe_{23}B_6$-type crystal, and crystal and glass interfacial energy. Our starting point is the set of experimental kinetic data and the analysis previously performed by the KJMA constant energy model and focused mainly at the beginning of the transformation where the nucleation frequency and growth rate are given by Eqs. (22) and (24), respectively. The major difficulty comes from the high homogeneous nucleation rate and high activation energies measured at temperatures ~30 K above T_g. Based on the melt fluidity observed at the ejection temperature in the melt spinning experiments and the viscosity value (10^{14} Pa s) at the glass transition temperature (T_g=862 K), only one adjustable parameter has to be introduced to fit the temperature dependence of the viscosity. Since the crystallization temperatures are above the Curie temperature of $Fe_{23}B_6$ and metastable melting of this phase must be approximately below the eutectic temperature (T_E=1414 K), a linear temperature dependence of ΔG is assumed (i.e., two adjustable parameters). Agreement between the model and experimental results requires a (linear) temperature dependence for the crystal-melt interfacial energy. The parameters introduced in the model to obtain the best fit with the experimental data are presented in Table III. The estimated temperature dependences of both the viscosity and interfacial energy are plotted in Figs. 13 and 14, respectively. The calculated transformation rate under a continuous heating rate is compared to the experimental one in Fig. 8.

As expected, the viscosity increases about 14 orders of magnitude from the eutectic temperature to the glass transition temperature. To allow a direct comparison with other glass forming liquids, the value of the fragility index m, defined by $m=E_\eta/kT_g$, with E_η the apparent activation energy of the viscosity at T_g, has been evaluated as m=78. Large values of m (60–150), indicative of the high apparent activation energy of the viscosity just above T_g, are attributed to fragile liquids by Böhmer and Angell.[45]

In the temperature interval explored experimentally (i.e., around 900 K) the interfacial energy has a value of ~80 mJ m^{-2} (see Fig. 14). This value is compared in Table IV to those estimated for other metallic glasses. All these

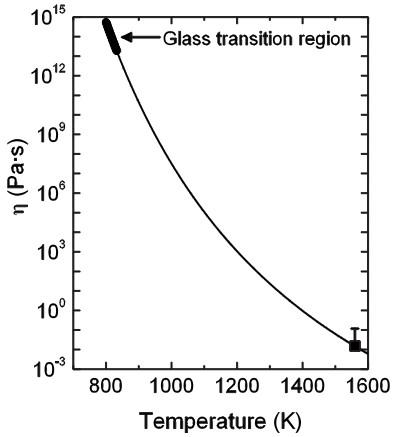

FIG. 13. Temperature dependence of the viscosity as fitted using the Fulcher-Vogel-Tammann equation (solid line). Estimated value of the liquid (symbol).

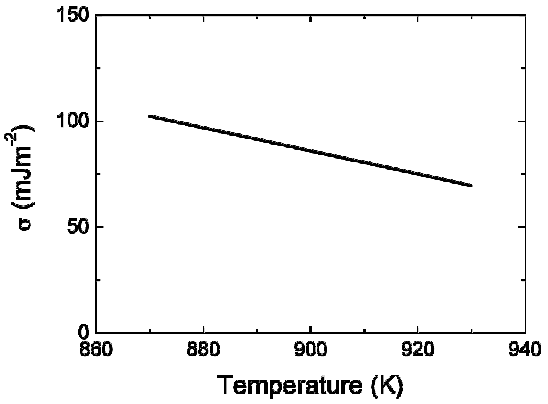

FIG. 14. Temperature dependence of the crystal-melt interfacial energy.

relatively low values of the interfacial energy promote a high nucleation frequency.[27,44]

C. Glass forming ability

GFA is one of the most important subjects in the study of BMGs, because it determines, to a large degree, the potential for this new category of materials to be utilized in various applications. Upon continuous cooling from its molten state, an alloy can eventually form a glass if, and only if, the cooling rate exceeds a critical value. This critical cooling rate R_c is a direct and universal measurement of the GFA of any substance and it has been shown to be directly related to the reduced glass transition temperature in metallic glasses.[1,49] Therefore, a complete understanding of GFA in this alloy should be supported by the evaluation of the value of its R_c. Since glass formation is a competing process against crystallization and its onset is controlled by nucleation and interface-controlled growth, these quantities have been used to obtain the transformation diagram.

The experimental values determined for the nucleation frequency and the interface-controlled crystal growth are shown in Fig. 15, as well as the calculated ones, as a function of temperature. It is worth pointing out the high value of the nucleation frequency in a large temperature interval with a maximum of about 10^{17} cm^{-3} s^{-1} at temperatures ~950 K, while the crystal growth rate remains rather low (10^{-7} cm s^{-1}) at these temperatures. Such a situation clearly favors the microstructure refinement, thus resulting in a nanocrystalline structure.

TABLE IV. Interfacial energy estimated from crystallization kinetic data in some metallic glasses.

Metallic glass	σ_S (mJ m^{-2})	Reference
$Fe_{40}Ni_{40}P_{14}B_6$	163	46
$Fe_{40}Co_{40}P_{14}B_6$	223	46
$Ni_{40}Pd_{40}P_{20}$	100	47
$Pd_{40}Cu_{30}Ni_{10}P_{20}$	61	48
$Zr_{41.2}Ti_{13.8}Cu_{12.5}Ni_{10}Be_{22.5}$	40	48
$Fe_{73.5}Si_{17.5}B_5Nb_3Cu_1$	131–136	26

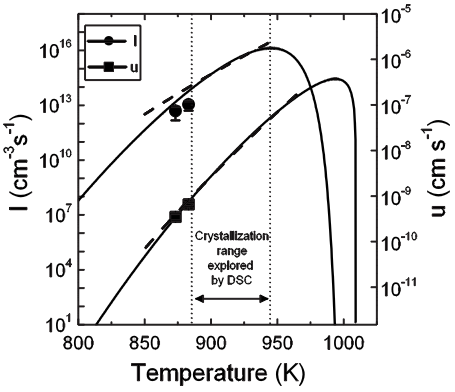

FIG. 15. Calculated values for the nucleation frequency and the interface-controlled crystal growth (solid lines) and the corresponding asymptotic values obtained using the constant activation energy kinetic model (dashed lines) versus temperature. Symbols correspond to experimental data.

The glass forming ability and thermal stability can be evaluated from these experimental and evaluated information.[27] Using the KJMA model, one can evaluate the TTT curve for the onset of nanocrystallization ($\alpha \ll 1$)—i.e., neglecting soft impingement. Under isothermal conditions the volume fraction crystallized after an annealing time t is given by

$$\alpha = f_1 x = f_1 \left[1 - \exp\left(- \frac{\pi I u^3 t^4}{3 f_1} \right) \right]. \tag{25}$$

Figure 16 shows the TTT curves obtained from Eq. (25) for a fixed value of α. The solid lines represent the results obtained with the nucleation/growth formalism for $\alpha = 1 \times 10^{-6}$ and 1×10^{-3}. The dashed curve is calculated with the constant activation energy model (derived in Sec. IV A) for $\alpha = 1 \times 10^{-6}$. Symbols represent the experimental evaluation of the time needed to transform the 0.1% volume

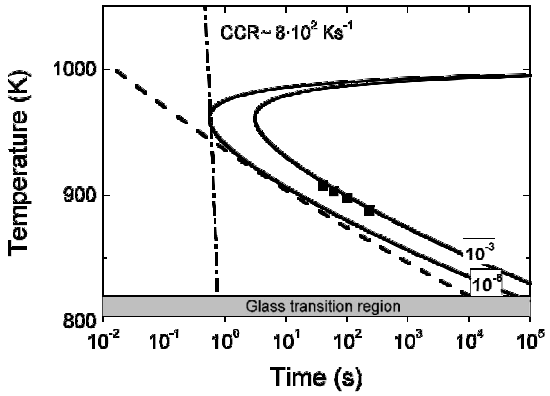

FIG. 16. The TTT diagram obtained using the constant activation energy kinetic model (dashed lines, $\alpha = 10^{-6}$) and the nucleation and growth KJMA formalism (solid lines, $\alpha = 10^{-6}$, 10^{-3}). Symbols: as fitted for $\alpha = 10^{-3}$ using the constant activation energy KJMA kinetic model. The dot-dashed line indicates the thermal path for a cooling rate of 8×10^2 K s^{-1}.

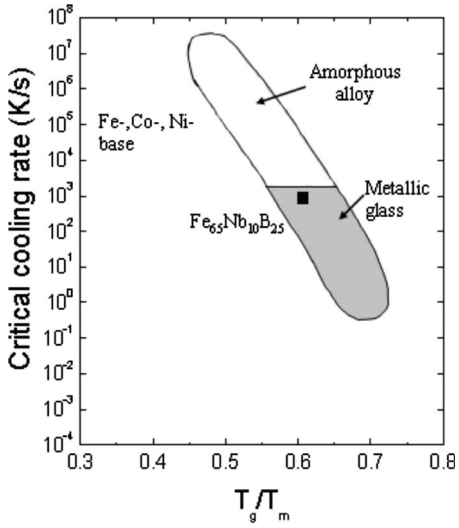

FIG. 17. Critical cooling rate as a function of the reduced glass transition temperature. Dashed area: experimental values reported in Ref. 1. Symbol: calculated value for $Fe_{65}Nb_{10}B_{25}$.

fraction from the kinetic analysis performed at 898, 903, and 908 K.

Typically, the critical cooling rate R_c is defined either by the cooling rate needed to obtain a crystalline fraction of $\alpha=1\times10^{-6}$ or by the nose of the corresponding TTT curve. Since the studied alloy has a composition very close to the one corresponding to the ternary eutectic of the Fe-FeNbB-Fe_2B system,[28] $T_m\approx T_E=1414$ K. Therefore, as shown in Fig. 16, the estimated value for this metallic alloy is $R_c\approx800$ K s^{-1}. This value and the corresponding value of the reduced glass transition temperature are compared in Fig. 17 with the already published data on the general relationship between R_c and T_{rg} for metallic alloys.[1] As expected, the results confirm that this alloy is a bulk glass former. Further, it should be mentioned that a ternary $Fe_{66}Nb_4B_{30}$ bulk metallic glass was recently obtained using copper-mould casting, where the alloy is cooled at about 100–500 K s^{-1}.[12] It is worth remarking, however, that the present estimate of the critical cooling rate is obtained considering that $Fe_{23}B_6$ is the only phase that precipitates during cooling.

V. CONCLUSIONS

The following conclusions are drawn from the present results.

(i) The $Fe_{65}Nb_{10}B_{25}$ metallic glass exhibits a wide supercooled region $\Delta T_x=51$ K, a high reduced glass transition temperature $T_{gr}\approx0.61$, and a low critical cooling rate $R_c\approx800$ K s^{-1}, which imply that this alloy is an excellent candidate as base composition for multicomponent BMGs.

(ii) The devitrification of the glassy ribbons by thermal treatment proceeds through the initial nanocrystallization of a $Fe_{23}B_6$-type phase, further precipitation of metastable Fe_3B, and finally of the stable bcc-Fe, Fe_2B, and FeNbB crystalline phases.

(iii) The coupling of isothermal and continuous heating DSC measurements demonstrate, via the master curve method, that nanocrystallization proceeds by nucleation and three-dimensional growth, initially interface controlled, with respective activation energies of $E_l=6.64$ eV and $E_u=4.81$ eV.

(iv) The progress of the transformation is explained by extension of the KJMA theory to include soft impingement. Assuming constant activation energy for the nucleation frequency, interface-controlled growth rate, and solute diffusion coefficient, values of the preexponential factors of these quantities are obtained that agree with the DSC kinetic data and values of nucleation frequency, growth rate, and maximum grain size determined experimentally from microstructural analysis at selected temperatures.

(v) Based on nucleation theory and initial interface-controlled growth, the solid-liquid interfacial energy is estimated to be $(577.0-54.56T)$ mJ m^{-2} by the use of a Vogel-Fulcher-Tamman temperature dependence of the supercooled liquid viscosity of the $Fe_{65}Nb_{10}B_{25}$ metallic alloy and a linear temperature dependence of the difference of the free energies in glassy and crystalline phase.

ACKNOWLEDGMENTS

This work was supported by Projects Nos. MAT2003-08271-C02, MAT2004-04761, and MAT2007-61521 granted by Spanish MEC and No. SGR2005-00201 granted by CIRIT (Catalunya). J.T.-S. would like to thank the MEC for a grant.

*Corresponding author: joan@vega.uab.es

[1] A. Inoue, Acta Mater. **48**, 279 (2000).
[2] M. E. McHenry, M. A. Willard, and D. E. Laughlin, Prog. Mater. Sci. **44**, 291 (1999).
[3] A. Inoue and A. Takeuchi, Mater. Trans., JIM **43**, 1892 (2002).
[4] T. Itoi and A. Inoue, Mater. Trans., JIM **40**, 643 (1999).
[5] M. Imafuku, S. Sato, H. Koshiba, E. Matsubara, and A. Inoue, Scr. Mater. **44**, 2369 (2001).
[6] B. Yao, L. Si, H. Tan, Y. Zhang, and Y. Li, J. Non-Cryst. Solids **332**, 43 (2003).
[7] M. Shapaan, J. Lábár, L. Lendvai, and L. K. Varga, Mater. Sci. Eng., A **375-377**, 789 (2004).
[8] A. Makino, K. Suzuki, A. Inoue, and T. Masumoto, Mater. Sci. Eng., A **179/180**, 127 (1994).
[9] A. Makino, T. Hatanai, A. Inoue, and T. Masumoto, Mater. Sci. Eng., A **226-228**, 594 (1997).
[10] Y. Naitoh, T. Bitoh, T. Hatanai, A. Makino, A. Inoue, and T. Masumoto, Nanostruct. Mater. **8**, 987 (1997).
[11] K. Suzuki, J. M. Cadogan, K. Aoki, A. P. Tsai, A. Inoue, and T. Masumoto, Scr. Mater. **44**, 1417 (2001).
[12] M. Stoica, K. Hajlaoui, A. Lemoulec, and A. R. Yavari, Philos. Mag. Lett. **86**, 267 (2006).

[13] S. Roth, M. Stoica, J. Degmova, U. Gaitzsch, J. Eckert, and L. Schultz, J. Magn. Magn. Mater. **304**, 192 (2006).
[14] B. Shen, C. Chang, and A. Inoue, Intermetallics **15**, 9 (2007).
[15] D. S. Song, J.-H. Kim, E. Fleury, W. T. Kim, and D. H. Kim, J. Alloys Compd. **389**, 159 (2005).
[16] A. N. Kolmogorov, Izv. Akad. Nauk SSSR, Ser. Mat. **3**, 355 (1937).
[17] W. A. Johnson and R. Mehl, Trans. AIME **185**, 416 (1939).
[18] M. Avrami, J. Chem. Phys. **7**, 1103 (1939); **8**, 212 (1940); **9**, 177 (1941).
[19] T. Pradell, D. Crespo, N. Clavaguera, and M. T. Clavaguera-Mora, J. Phys.: Condens. Matter **10**, 3833 (1998).
[20] J. S. Blazquez, C. F. Conde, and A. Conde, Acta Mater. **53**, 2305 (2005).
[21] Wei Lu, Biao Yan, and Wen-hai Huang, J. Non-Cryst. Solids **351**, 3320 (2005).
[22] S. Venkataraman, H. Hermann, C. Mickel, L. Schultz, D. J. Sordelet, and J. Eckert, Phys. Rev. B **75**, 104206 (2007).
[23] D. Jacovkis, Y. Xiao, J. Rodriguez-Viejo, M. T. Clavaguera-Mora, and N. Clavaguera, Acta Mater. **52**, 2819 (2004).
[24] D. Jacovkis, J. Rodriguez-Viejo, and M. T. Clavaguera-Mora, J. Phys.: Condens. Matter **17**, 4897 (2005).
[25] M. T. Clavaguera-Mora, N. Clavaguera, D. Crespo, and T. Pradell, Prog. Mater. Sci. **47**, 559 (2002).
[26] J. Ågren, M. T. Clavaguera-Mora, A. Costa e Silva, D. Djurovic, T. Gomez-Acebo, B.-J. Lee, Z.-K. Liu, P. Miodownik, and H. Seifert, CALPHAD: Comput. Coupling Phase Diagrams Thermochem. **31**, 53 (2007).
[27] M. T. Clavaguera-Mora, J. Alloys Compd. **220**, 197 (1995).
[28] J. Torrens-Serra, J. Rodríguez-Viejo, and M. T. Clavaguera-Mora, J. Non-Cryst. Solids **353**, 842 (2007).
[29] J. Torrens-Serra, P. Bruna, J. Rodríguez-Viejo, M. T. Clavaguera-Mora, and T. Pradell, *Industrial Applications of the Mössbauer Effect*, edited by M. Gracia, F. Plazaola, and J. F. Marco (Springer-Verlag, New York, 2005) [AIP Conf. Proc. **765**, 250 (2005)].
[30] P. Villars, A. Prince, and H. Okamoto, *Handbook of Ternary Alloy Phase Diagrams*, 1st ed. (ASM International, Materials Park, OH, 1995), Vol. 5.
[31] A. L. Greer, Acta Metall. **30**, 171 (1982).
[32] M. T. Clavaguera-Mora, N. Clavaguera, and J. Rodriguez-Viejo, Monatsch. Chem. **136**, 1947 (2005).
[33] N. Clavaguera, M. T. Clavaguera-Mora, and M. Fontana, J. Mater. Res. **13**, 744 (1998).
[34] A. T. W. Kempen, F. Sommer, and E. J. Mittemeijer, Acta Mater. **50**, 1319 (2002).
[35] M. Fontana, B. Arcondo, M. T. Clavaguera-Mora, and N. Clavaguera, J. Non-Cryst. Solids **353**, 2131 (2007).
[36] J. Farjas and P. Roura, Acta Mater. **54**, 5573 (2006).
[37] K. Suzuki, J. M. Cadogan, V. Shajwalla, A. Inoue, and T. Masumoto, Mater. Sci. Eng., A **226-228**, 554 (1997).
[38] A. S. Schaafsma, H. Snijders, F. van der Woude, J. W. Drijver, and S. Radelaar, Phys. Rev. B **20**, 4423 (1979).
[39] V. I. Tkatch, S. G. Rassolov, T. N. Moiseeva and V. V. Popov, J. Non-Cryst. Solids **351**, 1658 (2005).
[40] A. K. Gangopadhyay, T. K. Croat, and K. F. Kelton, Acta Mater. **48**, 4035 (2000).
[41] P. Bruna, D. Crespo, R. González-Cinca, and E. Pineda, J. Appl. Phys. **100**, 054907 (2006).
[42] Feng Liu and Gencang Yang, Acta Mater. **55**, 1629 (2007).
[43] J. W. Christian *The Theory of Transformations in Metals and Alloys* (Pergamon Press, Oxford, 1975).
[44] D. Turnbull, Contemp. Phys. **10**, 473 (1969).
[45] R. Böhmer and C. A. Angell, Phys. Rev. B **45**, 10091 (1992).
[46] V. I. Tkatch, A. M. Grishin, and S. I. Khartsev, Mater. Sci. Eng., A **337**, 187 (2002).
[47] Y. Nishi and K. Mikagi, Phys. Rev. B **34**, 1792 (1986).
[48] D. Xu and W. L. Johnson, Phys. Rev. B **74**, 024207 (2006).
[49] M. T. Clavaguera-Mora, Ber. Bunsenges. Phys. Chem. **102**, 1291 (1998).